Cite this: *Dalton Trans.*, 2019, **48**, 17298

## On the development of a new approach to the design of lanthanide-based materials for solution-processed OLEDs†

Makarii I. Kozlov,<sup>a</sup> Andrey N. Aslandukov,<sup>a</sup> Andrey A. Vashchenko,<sup>b</sup> Alexey V. Medvedko,<sup>a</sup> Alexey E. Aleksandrov,<sup>c</sup> Raitis Grzibovskis,<sup>d</sup> Alexander S. Goloveshkin,<sup>e</sup> Leonid S. Lepnev,<sup>b</sup> Alexey R. Tameev,<sup>c</sup> Aivars Vembris<sup>d</sup> and Valentina V. Utochnikova<sup>\*a,f</sup>

The targeted design of lanthanide-based emitters for solution-processed organic light-emitting diodes (OLEDs) resulted in obtaining an NIR OLED with one of the highest efficiencies among ytterbium-based solution-processed OLEDs ( $30 \mu\text{W W}^{-1}$ ). The design was aimed at the combination of high luminescence efficiency with solubility and charge carrier mobility. The latter was achieved thanks to the introduction of the purposefully selected neutral ligands, which combine electron mobility and the ability to sensitize lanthanide luminescence. Besides, the HOMO and LUMO energies and charge carrier mobility of solution-processed thin films of coordination compounds were measured experimentally for the first time, and novel highly luminescent europium-based materials with PLQYs of up to 80% and purely NIR luminescent ytterbium complexes were obtained.

Received 26th September 2019,  
Accepted 25th October 2019

DOI: 10.1039/c9dt03823j

rsc.li/dalton

## Introduction

Organic light-emitting diode (OLED) technology attracts increasing attention due to the possibility of obtaining high-surface area light sources and displays.<sup>1</sup> However, to make them commercially attractive, solution-processed OLEDs, which are cost-effective and allow high resolution, are important. Although examples of efficient solution-processed OLEDs exist,<sup>2,3</sup> allowing us to expect high prospects for this technology, the efficiency of these solution-processed OLEDs is usually lower than that of vacuum-deposited OLEDs.<sup>2,4</sup> Thus, the development of solution-processed OLEDs is an important task nowadays.

The design of efficient OLED materials should be aimed at the materials able to provide radiative relaxation of the triplet

excited state since according to the spin statistics 75% of electro-excitons possess triplet nature.<sup>5</sup> Nowadays there are several types of effective emitters, which are able to provide triplet harvesting, among which are the widely used iridium complexes<sup>6–8</sup> and rather promising TADF materials.<sup>9–11</sup> Despite the high efficiencies of OLEDs based on them, these types of emitters suffer from two drawbacks: high cost and high luminescence bandwidth (over 100 nm), which limit the contrast characteristics of the diodes. Another class of emitters that involve triplet levels in the luminescence process are lanthanide coordination compounds, which are well known for their narrow emission bands.<sup>12</sup> The position of lanthanide ionic luminescence bands depends only on the lanthanide ion, and by changing the lanthanide ion it is possible to obtain different colors of luminescence in the visible (for  $\text{Sm}^{3+}$ ,  $\text{Eu}^{3+}$ ,  $\text{Tb}^{3+}$ , and  $\text{Dy}^{3+}$  ions) and in the NIR ranges (for  $\text{Pr}^{3+}$ ,  $\text{Nd}^{3+}$ ,  $\text{Er}^{3+}$ ,  $\text{Tm}^{3+}$ , and  $\text{Yb}^{3+}$  ions). Among all the lanthanide complexes aromatic carboxylates are the most prospective materials for OLED applications due to their high chemical, thermal, optical, and electrical stability.<sup>13</sup> However, until recently, their use in OLEDs has been hampered by their insufficient solubility and charge transport properties.<sup>14,15</sup>

Another important challenge is obtaining OLEDs operating in the near-infrared (NIR) range, which have drawn particular interest in novel and cost-effective applications for emerging photonic and optoelectronic technologies, such as lab-on-chip platforms for medical diagnostics, flexible self-medicated pads for photo-

<sup>a</sup>M.V. Lomonosov Moscow State University, 1/3 Leninskiye Gory, Moscow, 119991, Russia. E-mail: valentina.utochnikova@gmail.com

<sup>b</sup>P.N. Lebedev Physical Institute, Leninsky prosp. 53, Moscow, 119992, Russia

<sup>c</sup>A.N. Frumkin Institute of Physical Chemistry and Electrochemistry, Leninsky prosp. 31, bld. 4, Moscow, 119071, Russia

<sup>d</sup>Institute of Solid State Physics, University of Latvia, 8 Kengaraga iela, Riga, LV-1063, Latvia

<sup>e</sup>A.N. Nesmeyanov Institute of Organoelement Compounds, Vavilova St. 28, Moscow, 119334, Russia

<sup>f</sup>EVOLED Ltd, 1A-24 Puškina iela, Riga LV-1050, Latvia

†Electronic supplementary information (ESI) available. See DOI: 10.1039/C9DT03823J

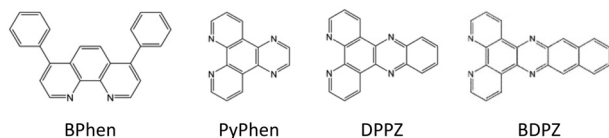


Fig. 1 The neutral ligands used in the present study.

dynamic therapy, night vision and plastic-based telecommunications, optical sensors and information processing.<sup>16–20</sup> Ytterbium compounds are the most promising NIR emitters for OLEDs since they combine rather high quantum yields and narrow emission bands. Despite their obvious importance, the efficiency of NIR OLEDs is still very low: the highest efficiency of a Yb-based solution-processed OLED reaches  $50 \mu\text{W W}^{-1}$ ,<sup>21</sup> while the typical value lies below  $10 \mu\text{W W}^{-1}$ .<sup>22–24</sup>

In the present paper we propose an approach to the design of emitter materials for solution-processed lanthanide-based OLED devices, in particular ytterbium-based. This approach is based on the purposeful selection of ligands for the lanthanide compounds, which are able to ensure (1) efficient lanthanide luminescence sensitization, (2) high charge carrier mobility, and (3) high solubility.

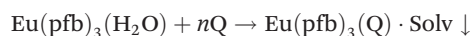
To ensure solubility the pentafluorobenzoate anion was selected as an anionic ligand, due to the high solubility of lanthanide pentafluorobenzoates in different organic solvents and even in water.<sup>25</sup> The derivatives of 1,10-phenanthroline (Fig. 1) were selected as neutral ligands, which combine electron transport properties and the sensitizing ability.

The chosen ligands BPhen, PyPhen, DPPZ and BDPZ are expected to possess high electron mobility due to their acceptor properties, heteroaromatic nature and high conjugation; moreover, BPhen is a well-known electron transport material.<sup>26</sup> The conjugation degree increases in the PyPhen–BPhen–DPPZ–BDPZ row, allowing us to expect a decrease in the triplet energy, and as a result DPPZ and BDPZ sensitize ytterbium luminescence in the NIR range, while BPhen and PyPhen sensitize europium luminescence in the visible region. Thus Yb(pfb)<sub>3</sub>(DPPZ) and Yb(pfb)<sub>3</sub>(BDPZ), as well as Eu(pfb)<sub>3</sub>(BPhen)·Solv and Eu(pfb)<sub>3</sub>(PyPhen), were investigated as materials for solution-processed OLEDs.

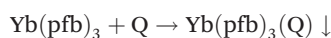
## Results and discussion

### Synthesis and characterization

Mixed-ligand complexes Eu(pfb)<sub>3</sub>(BPhen)·Solv and Eu(pfb)<sub>3</sub>(PyPhen) were obtained by the addition reaction by varying the reagent molar ratio  $n = 1$  or  $3$ :



Mixed-ligand complexes Yb(pfb)<sub>3</sub>(Q) (Q = DPPZ, BDPZ) were obtained by the addition reaction with the reagent molar ratio [Yb(pfb)<sub>3</sub>]:[Q] = 1:1:



The individuality and composition of the obtained compounds were determined based on PXRD data and TGA data along with mass detection and <sup>1</sup>H NMR spectroscopy.

Regardless of the initial reagent ratio  $n$ , the powder patterns of the obtained europium complexes were identical (Fig. 2): the positions of all the reflexes coincided, and a slight difference in the reflex intensity ratio seemed to be associated with the different degrees of texturing of the samples. The individuality of both europium and ytterbium complexes was proved by the indexing of the PXRD data (see ESI†). The absence of the reflexes corresponding to either Eu(pfb)<sub>3</sub>(H<sub>2</sub>O) and Yb(pfb)<sub>3</sub> or BPhen, PyPhen, DPPZ, and BDPZ indicates the absence of impurities in these reagents (Fig. 2). Thus, according to the PXRD data, individual complexes were formed, and their composition was independent of the initial ratio of the reagents.

The TGA data with evolved gas mass-detection and <sup>1</sup>H NMR spectroscopy were used to determine the number of neutral ligands and solvent molecules in the composition of the complexes. The TGA data of Eu(pfb)<sub>3</sub>(BPhen)·Solv (Fig. 3a) revealed that its decomposition occurs in three stages: first, in the range of 150–200 °C solvent molecules are eliminated, which results in the formation of Eu(pfb)<sub>3</sub>(BPhen). Then at 200 °C neutral ligand elimination begins, and after that thermal decomposition of the complex occurs with the formation of the oxide Eu<sub>2</sub>O<sub>3</sub>. Mass detection demonstrated the presence of ethanol molecules in the composition of the complex Eu(pfb)<sub>3</sub>(BPhen)·Solv in contrast to other complexes. By analyzing the first stage of weight loss, we determined that the complex contains water and ethanol solvent molecules, which correspond to the composition Eu(pfb)<sub>3</sub>(BPhen)·Solv, Solv = H<sub>2</sub>O + EtOH.

The TGA data of Eu(pfb)<sub>3</sub>(PyPhen), Yb(pfb)<sub>3</sub>(DPPZ), and Yb(pfb)<sub>3</sub>(BDPZ) complexes revealed the absence of coordinated solvent molecules as confirmed by the absence of weight loss and the corresponding ionic currents at temperatures below ca. 200 °C. The decomposition of all three complexes occurs in two stages: the first stage at ca. 150–250 °C corresponds to the elimination of the neutral ligands PyPhen, DPPZ and BDPZ, while at the second stage thermal decomposition of the complex occurs, and the weight loss ratio of the two stages corresponds to the ligand ratio [Q]:[pfb<sup>−</sup>] = 1:3 (Fig. 3b–d), thus showing that only one neutral ligand is coordinated by the lanthanide ion.

The ratio of [Q]:[pfb<sup>−</sup>] = 1:3 (Q = BPhen, PyPhen, DPPZ, BDPZ) in the complex composition was also confirmed by <sup>1</sup>H NMR spectroscopy. The <sup>1</sup>H NMR spectra of Eu(pfb)<sub>3</sub>(BPhen)·Solv, Eu(pfb)<sub>3</sub>(PyPhen) and Yb(pfb)<sub>3</sub>(Q) (Q = DPPZ, BDPZ) corresponded to the <sup>1</sup>H NMR spectra of Q = BPhen, PyPhen, DPPZ, and BDPZ, respectively, and were slightly broadened due to the effect of the Eu<sup>3+</sup> and Yb<sup>3+</sup> paramagnetic ions. The absence of protons in the anionic pfb<sup>−</sup> ligand does not allow the determination of the [pfb<sup>−</sup>]:[Q] ratio directly, and therefore we used <sup>1</sup>H NMR spectroscopy with an external standard.<sup>27</sup> Trioctylphosphine oxide (TOPO) was selected as an external standard, because it contains only

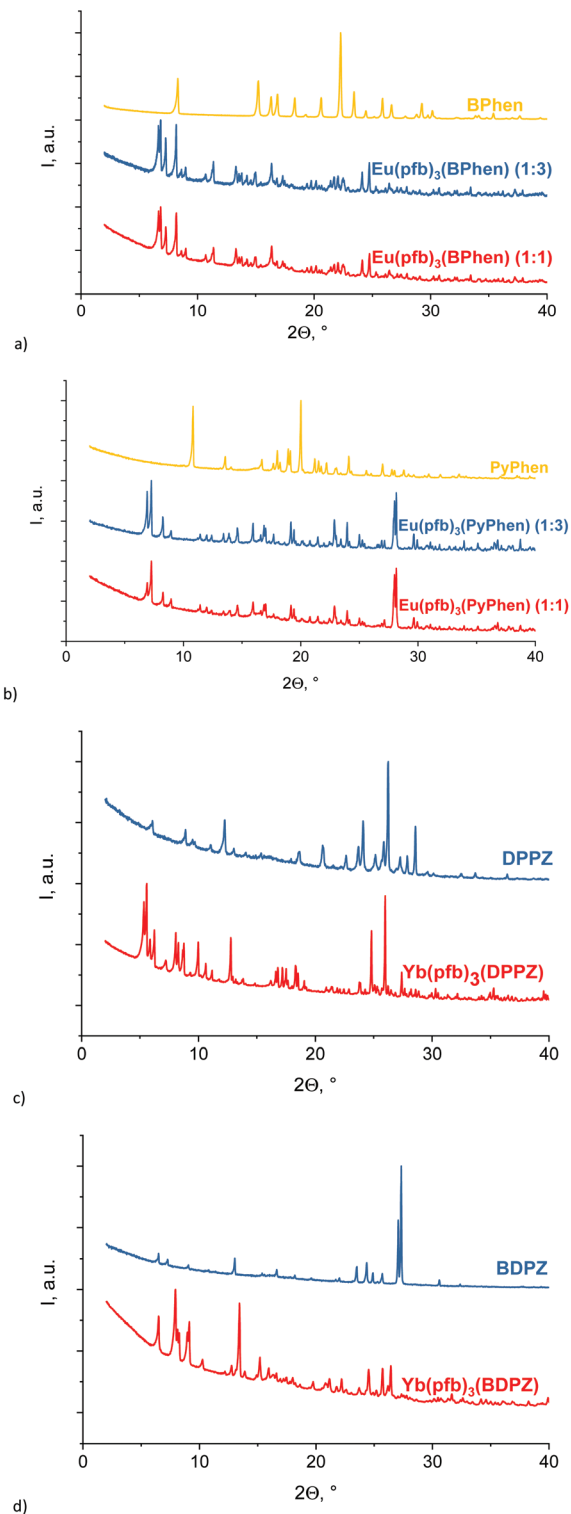


**Fig. 2** Normalized PXRD patterns of (a)  $\text{Eu}(\text{pfb})_3(\text{BPhen})\cdot\text{Solv}$ , (b)  $\text{Eu}(\text{pfb})_3(\text{PyPhen})$ , (c)  $\text{Yb}(\text{pfb})_3(\text{DPPZ})$ , and (d)  $\text{Yb}(\text{pfb})_3(\text{BDPZ})$ .

alkyl protons with the shifts in the range of 0–2 ppm which shall not overlap with the signals of the aromatic protons of the neutral ligands. The analysis of the integral intensity ratio of the signals of the neutral ligands  $Q = \text{BPhen}$ ,  $\text{PyPhen}$ ,  $\text{DPPZ}$ ,

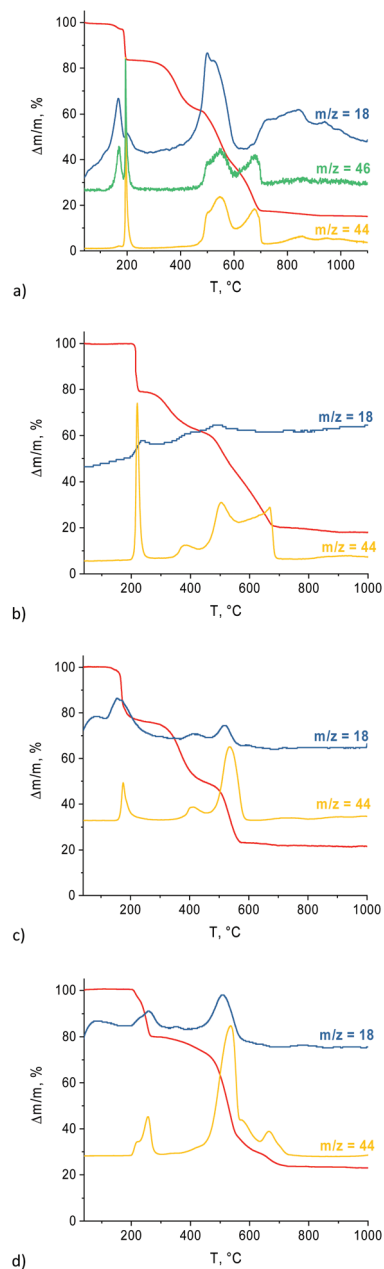


**Fig. 3** TGA curves (red) of (a)  $\text{Eu}(\text{pfb})_3(\text{BPhen})\cdot\text{Solv}$ , (b)  $\text{Eu}(\text{pfb})_3(\text{PyPhen})$ , (c)  $\text{Yb}(\text{pfb})_3(\text{DPPZ})$ , and (d)  $\text{Yb}(\text{pfb})_3(\text{BDPZ})$ . Normalized ionic currents are shown in blue ( $m/z = 18$ ), yellow ( $m/z = 44$ ), and green ( $m/z = 46$ ).

and  $\text{BDPZ}$  and the signals of  $\text{TOPO}$  in  $^1\text{H}$  NMR spectra confirmed that all the complexes contained one neutral ligand per lanthanide ion (Fig. 4 and Table 1).

### Luminescence properties

The selection of “neutral ligand–lanthanide ion” pairs is aimed at the possibility of the neutral ligand to sensitize the corresponding lanthanide luminescence, which depends primarily on the triplet state energy of the neutral ligand.<sup>28</sup> The values of triplet state energies (Table 2) were determined from

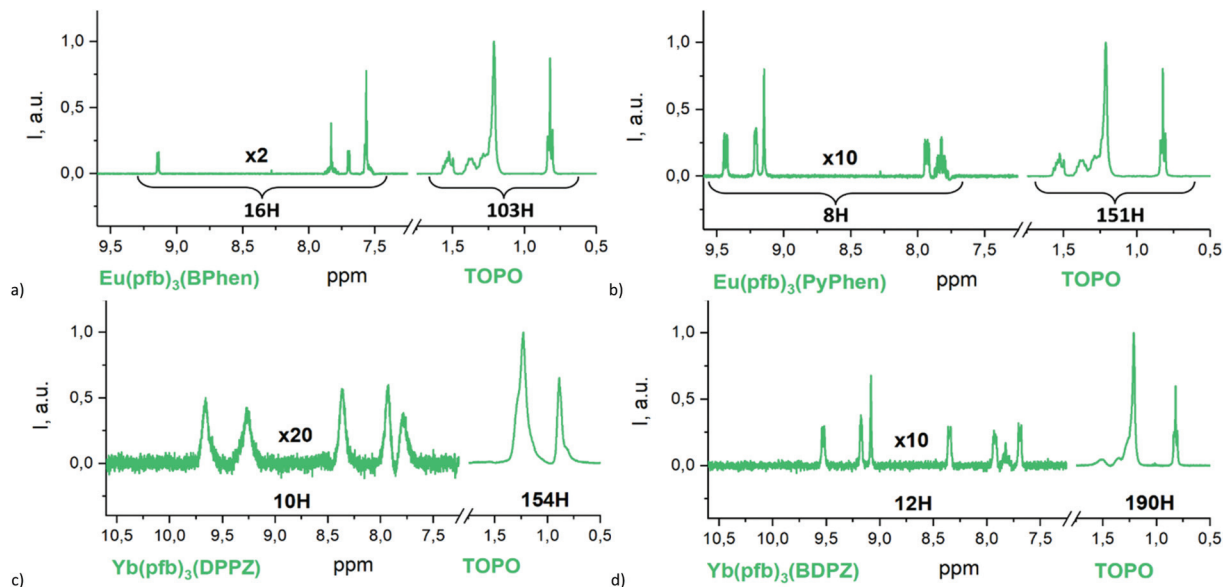


Fig. 4  $^1\text{H}$  NMR spectra of (a)  $\text{Eu}(\text{pfb})_3(\text{BPhen})\cdot\text{Solv}$ , (b)  $\text{Eu}(\text{pfb})_3(\text{PyPhen})$ , (c)  $\text{Yb}(\text{pfb})_3(\text{DPPZ})$ , and (d)  $\text{Yb}(\text{pfb})_3(\text{BDPZ})$  with an external standard (TOPO) in  $\text{DMSO}-d_6$  (a, b and d) and in  $\text{CDCl}_3$  (c).

Table 1 Integral intensity ratios of proton signals (calculated and found)

	The Q and TOPO proton signal ratios		
	Calculated for $\text{Ln}(\text{pfb})_3(\text{Q})$	Calculated for $\text{Ln}(\text{pfb})_3(\text{Q})_2$	Found
Q = BPhen	16 : 108	32 : 140	16 : 103
Q = PyPhen	8 : 152	16 : 187	8 : 152
Q = DPPZ	10 : 144	20 : 178	10 : 154
Q = BDPZ	12 : 183	24 : 236	12 : 190

the phosphorescence spectra of gadolinium complexes (see ESI<sup>†</sup>) and coincided well with the literature data.<sup>29</sup> Due to the increase of the conjugation length in the row PyPhen–BPhen–DPPZ–BDPZ, the energy of the triplet state expectedly decreases, and therefore both BPhen and PyPhen are able to sensitize the  $\text{Eu}^{3+}$  luminescence ( $E(^5\text{D}_0) = 17\,200\text{ cm}^{-1}$ ), while DPPZ and BDPZ triplet state energies are too low. However, they might be able to sensitize the luminescence of  $\text{Yb}^{3+}$  ( $E(^2\text{F}_{5/2}) = 10\,000\text{ cm}^{-1}$ ).

Indeed, both  $\text{Eu}(\text{pfb})_3(\text{BPhen})\cdot\text{Solv}$  and  $\text{Eu}(\text{pfb})_3(\text{PyPhen})$  possess typical europium ionic luminescence with no additional bands of ligand luminescence, and  $\text{Yb}(\text{pfb})_3(\text{Q})$  (Q = DPPZ and BDPZ) possess typical ytterbium ionic luminescence. It should be noted that the shape of the luminescence spectra depended both on the emitting ion and on the neutral

ligand (Fig. 5a), the latter indicating a slightly different coordination environment of the europium ions in  $\text{Eu}(\text{pfb})_3(\text{Q})\cdot\text{Solv}$  and the ytterbium ions in  $\text{Yb}(\text{pfb})_3(\text{Q})$ .

The excitation spectra of  $\text{Eu}(\text{pfb})_3(\text{BPhen})\cdot\text{Solv}$  and  $\text{Eu}(\text{pfb})_3(\text{PyPhen})$  indicate the crucial role of the neutral ligand in luminescence sensitization. Indeed, the spectra are dominated by the through-BPhen (band maximum at 360 nm) and through-PyPhen (band maximum at 340 nm) bands, while the through-pfb<sup>−</sup> excitation band (band maximum at 280 nm) is much less intense. Narrow excitation bands correspond to the direct through-europium excitation (Fig. 5b). The difference in the ratio between the through-europium and through-neutral ligand bands is probably connected with the different absorption coefficients of BPhen and PyPhen.

The quantum yield calculation demonstrated that the introduction of a neutral ligand results in a 3- to 4-fold increase of the luminescence efficiency compared to  $\text{Eu}(\text{pfb})_3(\text{H}_2\text{O})$ <sup>25</sup> reaching 55% (Table 3). The main reason for this is the high sensitization efficiency of BPhen and PyPhen, which reaches 100% for both ligands (Table 3). The complexes of BPhen,<sup>30,31</sup> including fluorobenzoates,<sup>32,33</sup> are known for their high quantum yields due to efficient through-BPhen sensitization, while PyPhen is less known to be an efficient sensitizer of europium luminescence.

The complex  $\text{Yb}(\text{pfb})_3(\text{BDPZ})$  could only be dissolved upon heating and at very low concentrations in strong donor and non-volatile solvents such as DMF and DMSO, which hinders

Table 2 Triplet state energies of the ligands and excited state energies of  $\text{Eu}^{3+}$ ,  $\text{Yb}^{3+}$

$\text{Eu}^{3+}$	$\text{Yb}^{3+}$	BPhen	PyPhen	DPPZ	BDPZ
$17\,200\text{ cm}^{-1}$	$10\,000\text{ cm}^{-1}$	$T_1 = 19\,900\text{ cm}^{-1}$	$T_1 = 21\,900\text{ cm}^{-1}$	$T_1 = 16\,400\text{ cm}^{-1}$	$T_1 = 14\,000\text{ cm}^{-1}$

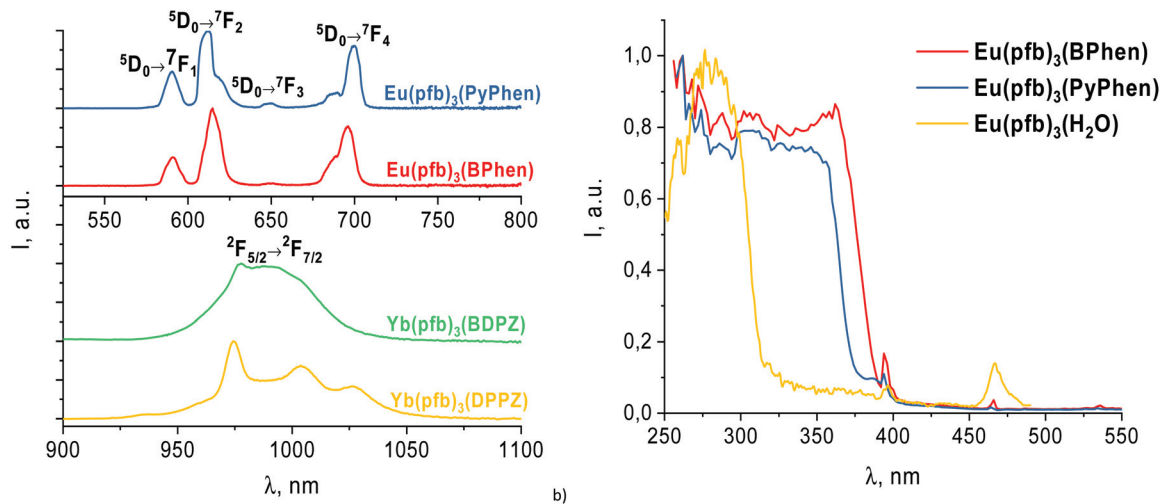


Fig. 5 (a) Normalized luminescence spectra of  $\text{Eu}(\text{pfb})_3(\text{BPhen})\text{-Solv}$ ,  $\text{Eu}(\text{pfb})_3(\text{PyPhen})$ ,  $\text{Yb}(\text{pfb})_3(\text{DPPZ})$ , and  $\text{Yb}(\text{pfb})_3(\text{BDPZ})$ . (b) Normalized excitation spectra of  $\text{Eu}(\text{pfb})_3(\text{BPhen})\text{-Solv}$ ,  $\text{Eu}(\text{pfb})_3(\text{PyPhen})$ , and  $\text{Eu}(\text{pfb})_3(\text{H}_2\text{O})$ .

Table 3 Luminescence properties of europium complexes

Complex	PLQY, %	$\tau_{\text{obs}}$ , ms	$\tau_{\text{rad}}^a$ , ms	$Q_{\text{Ln}}^{\text{Ln}}$ , % <sup>b</sup>	$\eta_{\text{sens}}^c$ , %
$\text{Eu}(\text{pfb})_3(\text{H}_2\text{O})^{25}$	15	0.65	1.0	65	23
$\text{Eu}(\text{pfb})_3(\text{BPhen})\text{-Solv}$	40	1.0	2.2	45	89
$\text{Eu}(\text{pfb})_3(\text{PyPhen})$	55	1.5	2.8	54	98

<sup>a</sup>  $\tau_{\text{rad}}^{-1} = 1465 \text{ s}^{-1} \times n^3 \times \frac{I_{\text{tot}}}{I_{0-1}}$ . <sup>b</sup>  $Q_{\text{Ln}}^{\text{Ln}} = \frac{\tau_{\text{obs}}}{\tau_{\text{rad}}} \times 100\%$ . <sup>c</sup>  $\text{PLQY} = \eta_{\text{sens}} \times Q_{\text{Ln}}^{\text{Ln}}$ .

the use of solution methods of research. So,  $\text{Yb}(\text{pfb})_3(\text{BDPZ})$  was excluded from further discussion.

### Mobility and boundary orbital energy determination

Materials for OLED emitters must possess not only high quantum yield, but also high charge carrier mobility, as well as appropriate energies of the HOMO and LUMO. The most common methods to determine frontier orbital energies are

either quantum chemical calculations or cyclic voltammetry (CV).<sup>34</sup> However, both methods provide a rather rough estimation: theoretical calculations are valid for single molecules under vacuum, while CV is carried out in solution, which also provides high error. The most practically significant values of frontier orbital energies for OLED applications are those experimentally determined for thin films, since the emitter is used in OLEDs in thin film form.

Therefore, in the present study the HOMO energies of  $\text{Eu}(\text{pfb})_3(\text{BPhen})$ ,  $\text{Eu}(\text{pfb})_3(\text{PyPhen})$ , and  $\text{Yb}(\text{pfb})_3(\text{DPPZ})$  were determined as the ionization energies of the films using the photoemission yield spectroscopy (PYS) method.<sup>35</sup> For  $\text{Yb}(\text{pfb})_3(\text{BDPZ})$  this measurement was impossible due to its insufficient film thickness and quality resulting from its low solubility.

Ionization energies calculated from the photoemission yield spectra  $Y^{2/5}(h\nu)$  of  $\text{Eu}(\text{pfb})_3(\text{BPhen})$ ,  $\text{Eu}(\text{pfb})_3(\text{PyPhen})$  (see ESI†), and  $\text{Yb}(\text{pfb})_3(\text{DPPZ})$  (Fig. 6a) are presented in Table 4. The obtained values are ca. 1.3 eV lower than those

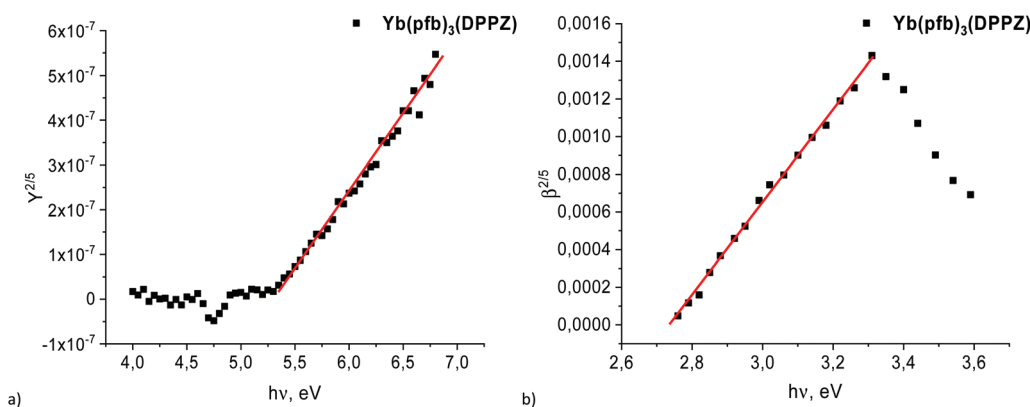


Fig. 6 (a) The photoemission yield of  $\text{Yb}(\text{pfb})_3(\text{DPPZ})$  depending on photon energy. (b) The spectral dependence of the quantum efficiency of photoconductivity  $\beta(h\nu)$  of  $\text{ITO}/\text{Yb}(\text{pfb})_3(\text{DPPZ})/\text{Al}$ .

**Table 4** HOMO, LUMO, and  $E_g$  energy values

	HOMO, eV	LUMO, eV	Energy gap, eV
Eu(pfb) <sub>3</sub> (BPhen)	5.2	1.7 <sup>a</sup>	n.a./3.5 <sup>b</sup>
Eu(pfb) <sub>3</sub> (PyPhen)	5.0	1.8 <sup>a</sup>	n.a./3.2 <sup>b</sup>
Yb(pfb) <sub>3</sub> (DPPZ)	5.3	2.7 <sup>c</sup>	2.6 <sup>d</sup> /3 <sup>b</sup>
Yb(pfb) <sub>3</sub> (BDPZ)	—	—	—

<sup>a</sup> Calculated as  $LUMO = HOMO - E_g^{exp}$ . <sup>b</sup>  $E_g^{exp}$  estimated from absorption spectra. <sup>c</sup> Measured from photoconductivity measurements. <sup>d</sup> Calculated as  $E_g = HOMO - LUMO^{exp}$ .

obtained for free BPhen, PyPhen, and DPPZ molecules,<sup>36,37</sup> due to complex formation. Expectedly, the HOMO energies of Eu(pfb)<sub>3</sub>(BPhen), Eu(pfb)<sub>3</sub>(PyPhen), and Yb(pfb)<sub>3</sub>(DPPZ) are mainly localized on the anionic ligand, as observed in ref. 29 for Eu(TTA)<sub>3</sub>(Q) (Q = PyPhen, DPPZ, BDPZ), where the HOMO energies of the complexes were also lower than the HOMO energies of PyPhen, DPPZ, and BDPZ. This indicates that the boundary orbital energy values of the neutral ligands cannot be used for those of the complexes containing these ligands.

The LUMO energy is calculated as  $LUMO = HOMO - E_g$ , where  $E_g$  is the HOMO–LUMO energy gap. The simplest method to determine  $E_g$  is from the beginning of the first absorption band,<sup>38,39</sup> but usually this value is overestimated if the direct HOMO–LUMO transition is forbidden. A more correct  $E_g$  value may be obtained from photoconductivity (PC) measurements,<sup>40</sup> however, this method requires thick (>500 nm) high quality smooth films, which cannot be obtained for nonvolatile compounds. In the present work we succeeded in obtaining films of enough quality for the photoconductivity measurements, but only for Yb(pfb)<sub>3</sub>(DPPZ) (Fig. 6b), while the  $E_g$  values of Eu(pfb)<sub>3</sub>(BPhen) and Eu(pfb)<sub>3</sub>(PyPhen) were obtained from absorption spectra (see ESI†). To verify the correctness of this experiment for this class of compounds, *i.e.* phenanthroline derivative containing ternary lanthanide pentafluorobenzoates, the  $E_g$  value of Yb(pfb)<sub>3</sub>(DPPZ) was calculated from both PC and absorption experiments. As expected, the real  $E_g$  value of Yb(pfb)<sub>3</sub>(DPPZ), obtained from PC data, is 0.4 eV lower than the value obtained from the absorption spectrum. This value can be considered as the experimental error of LUMO energy determination for the europium complexes.

Determination of charge carrier mobility for nonvolatile lanthanide complexes is usually impossible. Indeed, the “time-of-flight” method requires high thickness of the film (>1 μm),<sup>41</sup> which is impossible to obtain with high quality from solutions of small molecules. The mobility measurements of organic field-effect transistors (FETs) require the absence of charge carrier traps;<sup>42</sup> moreover, the FET mobility reflects the transport of charge carriers along the substrate, while in OLEDs charge carriers move across the film in the perpendicular direction to the substrate. Due to the morphology of the film (molecular orientation, packing, *etc.*), the mobility of charge carriers can be different in mutually perpendicular directions.<sup>43</sup> Even the photo-CELIV method,<sup>41</sup>

which is in principle suitable for thin films with low charge mobility, has never been successfully used for the solution processed films of the lanthanide complexes.

In the present work we succeeded in determining both the electron and hole mobilities of Eu(pfb)<sub>3</sub>(BPhen), which is the first example of such an experiment, while larger conjugation lengths of other neutral ligands allow us to expect that their mobilities exceed those of Eu(pfb)<sub>3</sub>(BPhen). The electron mobility of Eu(pfb)<sub>3</sub>(BPhen)  $\mu_e = 3.33 \times 10^{-5} \text{ cm}^2 \text{ V}^{-1} \text{ s}^{-1}$  is an order of magnitude larger than its hole mobility  $\mu_h = 1.87 \times 10^{-6} \text{ cm}^2 \text{ V}^{-1} \text{ s}^{-1}$ . This was expected since the mobility of the complex is due to the coordinated BPhen molecule, which is known to be an electron transport material ( $\mu_e(\text{BPhen}) = 3.22 \times 10^{-4} \text{ cm}^2 \text{ V}^{-1} \text{ s}^{-1}$ ).<sup>44</sup> It is however important to note that BPhen’s electron mobility is larger than that of Eu(pfb)<sub>3</sub>(BPhen), which makes the direct measurements of the mobility of the complex important instead of its estimation as the neutral ligand mobility value. At the same time the obtained  $\mu_e$  value is high enough and comparable to the  $\mu_e$  of electron transport materials such as TPBi.<sup>44</sup> Thus, the task of material design, combining high quantum yield and mobility, was fulfilled.

### Host selection

According to the mobility data complexes possess high electron and low hole mobilities. To increase the latter and thus to shift the recombination zone in the emitter film from the emitter/hole transport layer (HTL) border host:emitter films containing hole transporting hosts have to be used. In addition, to achieve good transport properties, these hosts have to ensure high efficiency energy transfer to the emitter material, which was investigated in the present section for the example of the Eu(pfb)<sub>3</sub>(BPhen) film.

As hole-transporting hosts commonly used CBP and TCTA were selected, as well as composite hosts CBP:OXD-7 (67:33 wt%) and CBP:TCTA (67:33 wt%), developed for solution-processed emitters.<sup>45</sup> Although OXD-7 is electron transporting and cannot be used in OLEDs alone, it was also tested to determine its sensitizing properties. Thus composite films host:Eu(pfb)<sub>3</sub>(BPhen) (10 wt%), as well as the pure Eu(pfb)<sub>3</sub>(BPhen) film, were deposited from chloroform.

The quantum yield of the pure Eu(pfb)<sub>3</sub>(BPhen) film equals 80%, which is higher than that of Eu(pfb)(BPhen)-Solv powder, obviously due to the absence of the coordinated quenching water molecules. The composite films demonstrated much lower quantum yields, with the highest yield (53%) obtained for OXD-7 and the lowest yield (~0%) obtained for TCTA, while for CBP, CBP:OXD-7, and CBP:TCTA the quantum yield was equal to 7% (Table 5). Therefore, CBP and

**Table 5** Quantum yields of host : emitter films, ±5%

Host	Pure	CBP	TCTA	OXD-7	CBP:OXD-7	CBP:TCTA
QY, %	80	7	0	53	7	7

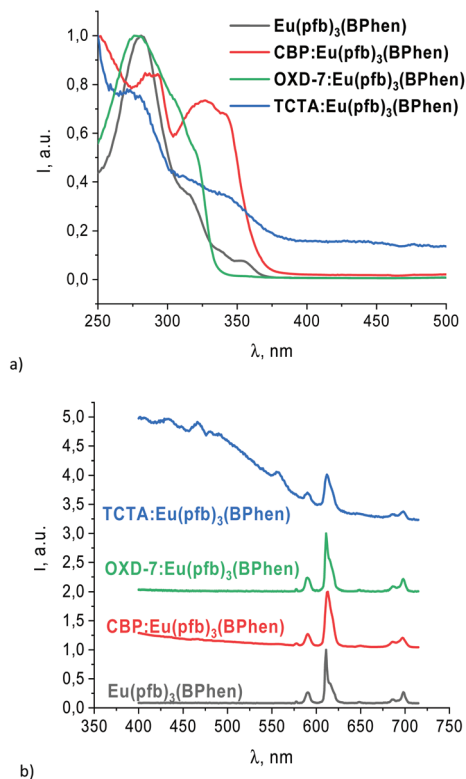


Fig. 7 Normalized (a) excitation and (b) luminescence spectra of composite films.

CBP:OXD-7 were selected as host materials for OLED fabrication (Fig. 7).

### OLED fabrication

Among the four obtained ternary complexes, one europium complex  $\text{Eu}(\text{pfb})_3(\text{BPhen})\cdot\text{Solv}$  and one ytterbium complex  $\text{Yb}(\text{pfb})_3(\text{DPPZ})$  were tested in OLEDs, because they combined all the required properties: high luminescence intensity, high electron mobility, and high solubility in a number of low boiling temperature solvents, *i.e.* chloroform, acetone, THF, *etc.*

Initially red-emitting  $\text{Eu}(\text{pfb})_3(\text{BPhen})\cdot\text{Solv}$  was tested in OLEDs; HTL and ETL layers were selected based on the values of HOMO and LUMO energies (Table 6). OLED A, based on a host-free  $\text{Eu}(\text{pfb})_3(\text{BPhen})$  emissive layer, demonstrated typical ionic europium luminescence and rather high current density (Fig. 9) thanks to the purposeful combination of high quantum yield and electron mobility. However, its luminance was low due to both solution processing and low hole mobility. Indeed, the use of the composite CBP: $\text{Eu}(\text{pfb})_3(\text{BPhen})$  (50 wt%) film (OLED B) demonstrated higher luminance despite a much lower quantum yield, showing the crucial importance of the transport properties of the materials for OLED applications. However, an additional wide luminescence band in the EL spectrum of OLED B, corresponding to the superposition of the luminescence of TPBi and poly-TPD layers, and the presence of a hump in the  $I$ - $V$  curve of OLED B indicate imbalanced hole and electron currents, showing that

Table 6 Europium-based OLED heterostructures, as well as switch-on voltage and maximum luminance values

Device	Heterostructure	$U_{\text{on}}$ , V	Maximum luminance, $\text{cd m}^{-2}$
A	ITO/PEDOT : PSS/poly-TPD/ $\text{Eu}(\text{pfb})_3(\text{BPhen})$ /TPBi/LiF/Al	7	n/a
B	ITO/PEDOT : PSS/poly-TPD/CBP : $\text{Eu}(\text{pfb})_3(\text{BPhen})$ (50 wt%)/TPBi/LiF/Al	4	2 (10–12 V)
C	ITO/PEDOT : PSS/poly-TPD/CBP : $\text{Eu}(\text{pfb})_3(\text{BPhen})$ (50 wt%)/OXD-7/LiF/Al	5	2 (10–12 V)
D	ITO/PEDOT : PSS/poly-TPD/CBP (60 wt%):OXD-7 (30 wt%): $\text{Eu}(\text{pfb})_3(\text{BPhen})$ (10 wt%)/OXD-7/LiF/Al	5	9 (17 V)

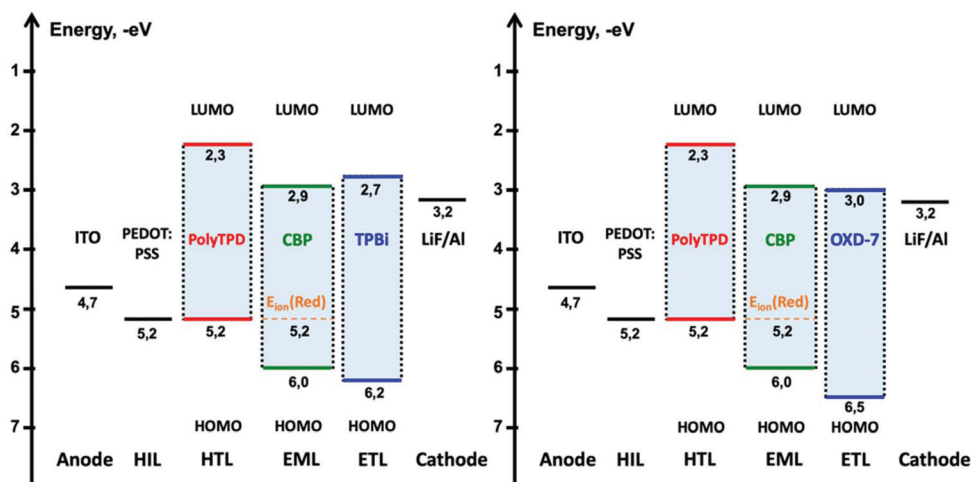


Fig. 8 The energy diagram of europium OLEDs, Red =  $\text{Eu}(\text{pfb})_3(\text{BPhen})$ .

the OLED heterostructure was not optimal. The replacement of the ETL material TPBi by OXD-7, which possesses suitable HOMO and LUMO energies (Fig. 8), allowed us to obtain OLED C, which demonstrated pure ionic europium luminescence and balanced currents. Further optimization, *i.e.* host and host : emitter ratio variation, allowed us to achieve a luminance of  $9 \text{ cd m}^{-2}$  for almost pure europium emission of OLED D (Table 6).

Similarly, OLED F, based on the pure  $\text{Yb}(\text{pfb})_3(\text{DPPZ})$  film, demonstrated typical ytterbium luminescence in the NIR range and high current density, while the introduction of the hole-transporting host material CBP led to an increase in its efficiency of up to  $30 \mu\text{W W}^{-1}$  (Fig. 10). This is one of the highest values for the solution-processed Yb-based OLEDs, which was exceeded only once in ref. 21, where an efficiency of  $50 \mu\text{W W}^{-1}$  was reached (Table 7).

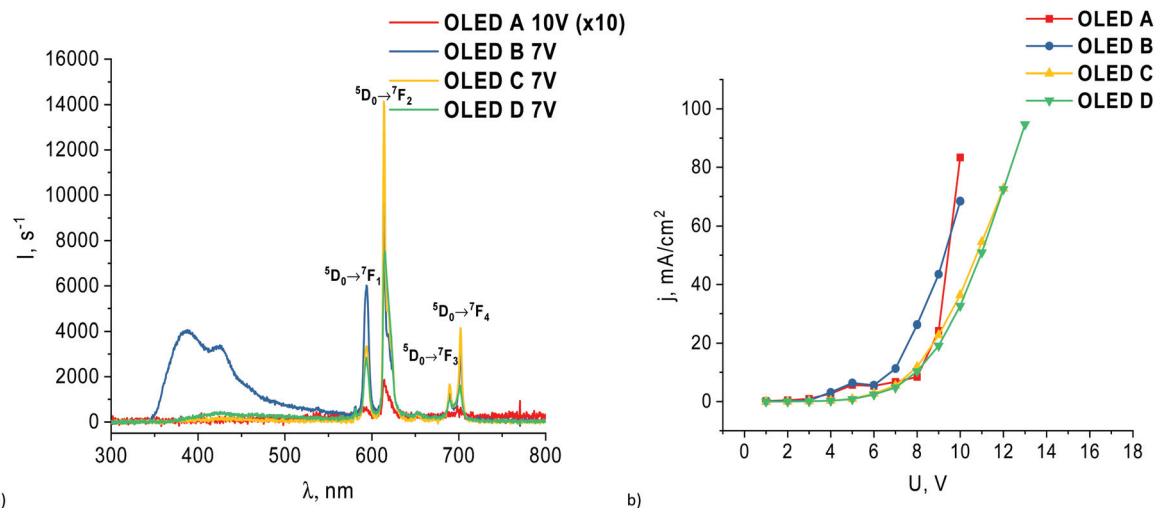


Fig. 9 (a) Electroluminescence spectra and (b)  $I$ - $V$  curves of OLEDs A, B, C, D, and E.

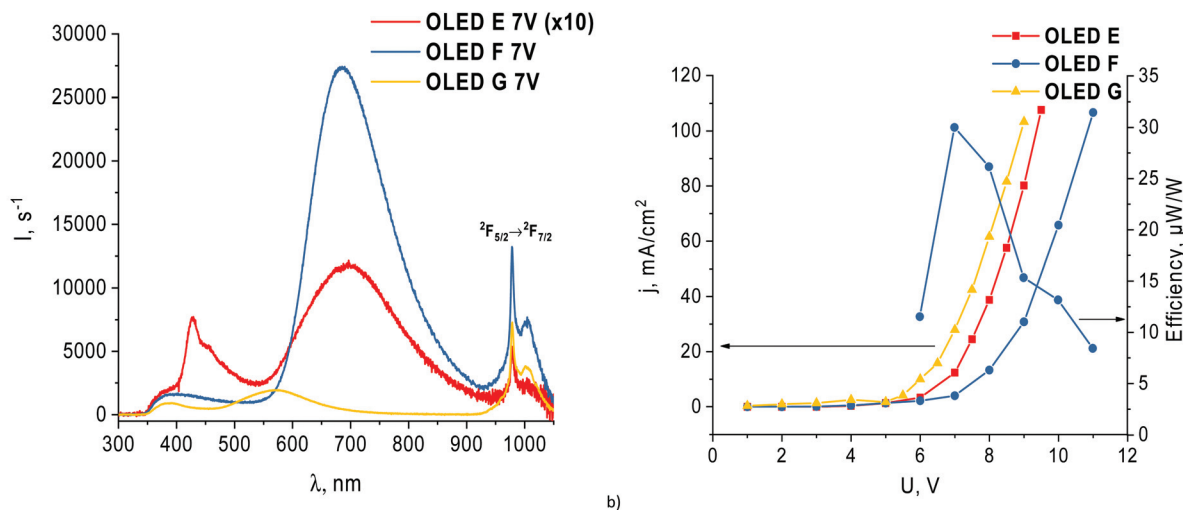


Fig. 10 (a) Electroluminescence spectra and (b)  $I$ - $V$  curves of OLEDs E, F, and G.

Table 7 Ytterbium-based OLED heterostructures, as well as switch-on voltage and maximum efficiencies

Device	Heterostructure	$U_{\text{on}}$ , V	Efficiency, $\mu\text{W W}^{-1}$
E	ITO/PEDOT : PSS/poly-TPD/ $\text{Yb}(\text{pfb})_3(\text{DPPZ})/\text{TPBi}/\text{LiF}/\text{Al}$	6	n/a
F	ITO/PEDOT : PSS/poly-TPD/CBP : $\text{Yb}(\text{pfb})_3(\text{DPPZ})$ (50 wt%)/TPBi/LiF/Al	4	30
G	ITO/PEDOT : PSS/CBP : $\text{Yb}(\text{pfb})_3(\text{DPPZ})$ (50 wt%)/TPBi/LiF/Al	5	n/a

## Experimental section

### Materials and methods

All solvents and chemicals were purchased from commercial sources.

$^1\text{H}$  NMR spectra were recorded at 25 °C using an Agilent 400 MR spectrometer with an operating frequency of 400.130 MHz. Chemical shifts are reported in ppm relative to  $\text{Me}_4\text{Si}$  ( $^1\text{H}$ ). Thermal analysis was carried out on a thermoanalyzer STA 409 PC Luxx (NETZSCH, Germany) in the temperature range of 20–1000 °C in air and at a heating rate of 10°  $\text{min}^{-1}$ . The evolved gases were simultaneously monitored during the TA experiment using a coupled QMS 403C Aeolos quadrupole mass spectrometer (NETZSCH, Germany). The mass spectra were registered for the species with the following  $m/z$  values: 18 (corresponding to  $\text{H}_2\text{O}$ ), 44 (corresponding to  $\text{CO}_2$ ) and 46 (corresponding to  $\text{C}_2\text{H}_5\text{OH}$ ).

Powder X-ray diffraction (PXRD) was performed by using Bruker D8 Advance [ $\lambda(\text{Cu-K}\alpha) = 1.5418 \text{ \AA}$ ; Ni filter] and Bruker D8 Advance Vario diffractometers [ $\lambda(\text{Cu-K}\alpha_1) = 1.54060 \text{ \AA}$ ; Ge(111)-monochromator] with a step size of 0.020°. The patterns were indexed by using SVD-Index<sup>46</sup> as implemented in the TOPAS 4.2 software.<sup>47</sup> Then, the powder patterns were refined by using the Pawley method.

Emission and excitation spectra were recorded using a FluoroMax Plus spectrophotometer upon excitation with a xenon lamp. Luminescence lifetime measurements were recorded and detected on the same system. The lifetimes are the averages of at least three independent measurements. All luminescence decays proved to be perfect single-exponential functions. Photoluminescence quantum yields in the visible range were determined with the FluoroMax Plus spectrophotometer at room temperature upon excitation into ligand states according to an absolute method using an integration sphere. The modified de Mello *et al.*<sup>48</sup> method requires the measurement of (i)  $L_a$ , the integrated intensity of light exiting the sphere when the empty cuvette is illuminated at the excitation wavelength (Rayleigh scattering band); (ii)  $L_c$ , the same integrated intensity at the excitation wavelength when the sample is introduced into the sphere; (iii)  $E_a$  the integrated intensity of the entire emission spectrum of the empty cuvette; and (iv)  $E_c$  the integrated intensity of the entire emission spectrum of the cuvette with the sample. The absolute quantum yield is then given by:

$$\text{PLQY} = \frac{E_c - E_a}{L_a - L_c} \times 100\%$$

Photoemission yield spectroscopy (PYS) was carried out using a custom-made system to determine the ionization energy of the thin films. The sample and a copper electrode which collected the emitted electrons were placed in a vacuum chamber. During the measurement a pressure of  $1 \times 10^{-5}$  mbar was ensured in the chamber. There was an about 2 cm gap between the copper electrode and the sample. An ENERGETIQ Laser Driven Light Source (LDLSEQ-99) was used as the light source. The wavelength with a spectral width of

2 nm was changed using an MYM-1 diffraction grating monochromator. The light/dark cycles were switched using a Newport 76993 shutter. The sample was irradiated through the  $2 \times 15$  mm slit in the copper electrode. A short focal length cylindrical lens was placed between the monochromator and the quartz window of the vacuum cryostat providing illumination of the  $5 \times 15$  mm large area of the sample. A voltage of 50 V was applied to the electrodes to improve the precision of the measurement as the signal was amplified by one order of magnitude compared to the signal without applied voltage. The ITO electrode under the organic film precluded the charging of the sample which could have decreased the signal quality. A Keithley617 electrometer with a built-in voltage source was used to apply the voltage as well as to measure the electrical current. Photoemission yield  $Y(h\nu)$  was calculated as:

$$Y(h\nu) = \frac{I(h\nu)}{P(h\nu)},$$

where  $I(h\nu)$  is the number of emitted electrons and  $P(h\nu)$  is the number of incident photons with the energy of  $h\nu$ .

The relationship between photoemission yield and ionization energy  $E_{\text{ioniz}}$  can be expressed as a power law:

$$Y(h\nu) = \alpha(h\nu - E_{\text{ioniz}})^n,$$

where  $\alpha$  is the constant showing the amplitude of the signal and  $n = 1\text{...}3$  depending on the studied materials.<sup>49</sup> The value of  $n = 2$  is used in the case of metals,<sup>50,51</sup> while  $n = 2.5\text{...}3$  is used in the case of semiconductors.<sup>52,53</sup> The value  $n = 2.5$  was used in the present paper. To obtain  $E_{\text{ioniz}}$ ,  $Y^{1/n}(h\nu)$  was calculated and plotted depending on photon energy. The linear part of the  $Y^{1/n}(h\nu)$  curve was extrapolated until  $Y^{1/n}(h\nu) = 0$  which allowed the calculation of the ionization energy of the studied compound.

The absorption spectra of the thin films were recorded using an Ocean Optics HR4000CG-UV-NIR spectrometer in the measurement range between 200 nm and 1100 nm.

The adiabatic energy gap  $E_g$  of the studied compounds was determined from the photoconductivity measurements using a similar setup as for the PYS measurements. Instead of the electron collecting electrode, we used an aluminum electrode deposited on the film of the investigated complex (ITO/complex/Al).

The threshold energy of photoconductivity  $E_{\text{th}}$  can be estimated from the spectrum of the quantum efficiency of the photoconductivity  $\beta(h\nu)$ . The value of  $\beta(h\nu)$  was estimated according to the equation:<sup>54</sup>

$$\beta(h\nu, U) = \frac{j_{\text{ph}}(h\nu, U)}{k(h\nu)I(h\nu)g(h\nu)}, \quad (1)$$

where  $j_{\text{ph}}$  is the density of photocurrent at a given photon energy  $h\nu$  and applied voltage  $U$ ,  $I(h\nu)$  is the intensity of light (phot per  $\text{cm}^2$  per s),  $k(h\nu)$  is the transmission of the semitransparent electrode,  $g(h\nu)$  is the coefficient that characterizes the absorbed light in the organic layer.

It has been shown that in anthracene-type crystals the spectral dependence of  $\beta(h\nu)$  in the near threshold region can be approximated using:<sup>54</sup>

$$\beta(h\nu) = A(h\nu - E_{\text{th}})^n, \quad (2)$$

where  $n \approx 5/2$ ,  $E_{\text{th}}$  is the threshold of intrinsic conductivity and  $A$  is the coefficient. The value of the photoconductivity threshold  $E_{\text{th}}$  correlates with the value of the adiabatic energy gap.<sup>54</sup>

The mobility of the thin films was measured using the MIS-CELIV method, which consists in registering a transient current signal with a linearly increasing voltage of the electric field applied to the sample.<sup>55,56</sup> Samples for determining mobility were prepared as follows: a glass substrate with indium tin oxide (ITO) coated with a dielectric layer of SiO<sub>2</sub> (70 nm) was successively applied as a layer of the test compound ( $d = 100$  nm) and an aluminum layer (80 nm) as the opposite electrode. The SiO<sub>2</sub> layer is blocking for both types of charge carriers, *i.e.* it prevents carrier injection from ITO. When measuring the transient current of holes, a linearly increasing positive potential was applied to ITO; therefore, extraction of holes took place on the aluminum electrode. The SiO<sub>2</sub> layer prevented the injection of holes from the ITO electrode. In this case, the contribution of the electron current to the signal can be neglected, since the SiO<sub>2</sub> layer also blocked it. To measure the electron mobility, the polarity of the voltage applied to the sample was reversed.

The characteristic time  $t_{\text{max}}$  corresponding to the maximum transient current value was determined from the transient current curve. Typical transient current signals in the layers of organic semiconductors prepared by casting from a solution were previously described.<sup>56</sup> The mobility of charge carriers ( $\mu$ ) was calculated according to the formula (3).

$$\mu = \frac{2 \times d^2}{A \times (t_{\text{max}})^2}, \quad (3)$$

where  $d$  is the thickness of the compound layer and  $A$  is the applied voltage ramp rate.

### OLED manufacture

Prepatterned indium tin oxide coating with 15 Ohm per sq on the glass substrates (Lumtec Corp.) were used as anodes. were used as anodes. The substrates were sequentially washed in an ultrasonic bath with NaOH solution (30 min), distilled water (10 min), and 2-propanol (10 min) and then dried under a flow of N<sub>2</sub>. Then a 30 minute UV-treatment was performed in order to remove residual organic impurities.

All the spin-coating deposition processes were performed under ambient air conditions. A 50 nm-thick PEDOT:PSS (poly(3,4-ethylenedioxythiophene):poly(styrenesulfonate), Lumtec Corp.) hole-injection layer was deposited by pouring 300  $\mu$ l of the solution onto the substrate, followed by rotation for 1 min at 2000 rpm. The obtained film was dried at 100 °C for 30 min. A 20 nm-thick hole-transporting poly-TPD (Ossila) was spin-coated from chlorobenzene (5 g L<sup>-1</sup> concentration) at 2000 rpm for 1 min and then dried at 100 °C for 10 min.

Finally, emission layers were spin-coated from chloroform ( $c = 7$  g L<sup>-1</sup> for europium complexes and 5 g L<sup>-1</sup> for ytterbium complexes) at 1500 rpm for 1 min.

After deposition the substrates were transferred into an argon glove box where emission layers were dried at 80 °C for 20 minutes. The ~20 nm-thick electron-transporting/hole-blocking layers TPBi (Lumtec Corp.) and OXD-7 (Ossila) were thermally evaporated (Univex-300, LeyboldHeraeus) followed by an ~1 nm-thick LiF layer and a >100 nm-thick aluminum layer as the cathode under a pressure of below 10<sup>-5</sup> mbar. The thicknesses of the layers were controlled by a quartz microbalance resonator pregraded by atomic force microscopy.

Measurements of the OLED characteristics were performed in the argon glove box. Electroluminescence spectra were obtained using an Ocean Optics Maya 2000 Pro CCD spectrometer sensitive within 200–1100 nm.  $I$ - $V$  curves were measured using two DT 838 digital multimeters. The luminance was measured using a TKA-PKM luminance meter (TKA Instruments). OLED NIR luminance power was determined using a precalibrated Coherent FieldMaxII Laser Power Meter with an optical filter removing the visible part of the spectra. NIR efficiency was calculated as the ratio of measured luminance power to consumed electrical power.

### Synthesis

**Synthesis of PyPhen, DPPZ, and BDPZ ligands.** The starting compound 1,10-phenanthroline-5,6-dione was synthesized according to the literature<sup>57</sup> with 64% yield.

**PyPhen.**<sup>58</sup> 1,10-Phenanthroline-5,6-dione (876 mg, 4.17 mmol) was stirred with 1,2-ethylenediamine (0.877 ml, 13.14 mmol) and methanol (44 ml) for 24 h at rt. The red solution was evaporated to dryness. The residue was recrystallized from toluene. Yield 741 mg (77%) of a yellow solid.

<sup>1</sup>H-NMR (CDCl<sub>3</sub>) 7.80 (dd, <sup>3</sup>J 8.0, 8.2 Hz, 2H), 9.00 (s, 2H), 9.30 (dd, <sup>3</sup>J 4.4 Hz, 2H), 9.50 (dd, <sup>3</sup>J 8.0, 8.2 Hz, 2H).

**DPPZ.**<sup>59</sup> 1,10-Phenanthroline-5,6-dione (1.050 g, 5 mmol) was mixed with *o*-phenylenediamine (0.595 g, 5.5 mmol) and *p*-TsOH·H<sub>2</sub>O (9.5 mg, 0.05 mmol) and refluxed in dry ethanol (15 ml) for 8 h. The reaction mixture was cooled down to rt and filtered off. The obtained powder was recrystallized from the ethanol-water mixture. Yield 1.222 g (87%) of yellow powder.

<sup>1</sup>H-NMR (DMSO-d<sub>6</sub>) 7.88–7.91 (m, 2H), 8.01–8.03 (m, 2H), 8.30–8.33 (m, 2H), 9.17–9.18 (m, 2H), 9.43–9.45 (m, 2H).

**BDPZ.** 1,10-Phenanthroline-5,6-dione (0.840 g, 4 mmol) was mixed with naphthalene-1,2-diamine (0.695 g, 4.4 mmol) and *p*-TsOH·H<sub>2</sub>O (7.6 mg, 0.04 mmol) and refluxed in dry ethanol (35 ml) for 8 h. The reaction mixture was cooled down to rt, filtered off, and washed with 30 ml of methanol. An orange powder was recrystallized from DMF, filtered off and washed with diethyl ether. Yield 1.106 g (83%) of orange foam.

<sup>1</sup>H-NMR (CDCl<sub>3</sub>) 7.62–7.66 (m, 2H), 7.80 (dd, <sup>3</sup>J 8.1 Hz, 2H), 8.20–8.23 (m, 2H), 8.96 (s, 2H), 9.25–9.26 (dd, <sup>3</sup>J 4.4 Hz, 2H), 9.65 (dd, <sup>3</sup>J 8.1 Hz, 2H).

**Synthesis of Eu(pfb)<sub>3</sub>(H<sub>2</sub>O) and Yb(pfb)<sub>3</sub> complexes.** An excess of concentrated aqueous solution of NH<sub>3</sub> (6.5 ml, 20.0 equiv.) was added to an aqueous solution of LnCl<sub>3</sub>·6H<sub>2</sub>O (Ln =

Eu, Yb) (5 mmol, 1 equiv.) in water (25 ml). The mixture was stirred for 30 min, and the precipitate of  $\text{Ln}(\text{OH})_3$  (Ln = Eu, Yb) was centrifuged and washed with water until the pH of the washing solution became neutral. A small excess of freshly prepared  $\text{Ln}(\text{OH})_3$  was placed in a beaker, and a solution of 2,3,4,5,6-pentafluorobenzoic acid (12.5 mmol, 2.5 equiv.) in ethanol (25 ml) was added. The reaction mixture was stirred for 1 h at 60 °C and the unreacted components were separated by filtration followed by the evaporation of the clear solution to dryness. Yield 90% of white powder. – CHN:  $\text{Eu}(\text{pfb})_3(\text{H}_2\text{O})$ , calcd, % C 31.40, H 0.25, found C 31.32, H 0.34,  $\text{Yb}(\text{pfb})_3$ , calcd, % C 31.28, found C 31.38.

**Synthesis of  $\text{Eu}(\text{pfb})_3(\text{BPhen})\cdot\text{Solv}$  and  $\text{Eu}(\text{pfb})_3(\text{PyPhen})$ .** The solution of  $\text{Eu}(\text{pfb})_3(\text{H}_2\text{O})$  (1 mmol) in 20 ml of ethanol was added to the solution of one or three equivalents of Q = BPhen and PyPhen (1 mmol or 3 mmol) in 30 ml of ethanol. The reaction mixture was refluxed for 24 h and then was evaporated to half-volume until precipitate formation. The precipitate was filtered off, washed with ethanol, and dried in air. Yield 70% of white powders  $\text{Eu}(\text{pfb})_3(\text{BPhen})\cdot\text{Solv}$  and  $\text{Eu}(\text{pfb})_3(\text{PyPhen})$ . – CHN:  $\text{Eu}(\text{pfb})_3(\text{BPhen})\cdot\text{Solv}$  (1 : 1), calcd, % C 48.36, H 1.44, N 2.51, found C 48.48, H 1.60, N 2.43,  $\text{Eu}(\text{pfb})_3(\text{PyPhen})$  (1 : 1), calcd, % C 41.32, H 0.79, N 5.51, found C 41.19, H 0.96, N 5.66,  $\text{Eu}(\text{pfb})_3(\text{BPhen})\cdot\text{Solv}$  (1 : 3), calcd, % C 48.36, H 1.44, N 2.51, found C 48.54, H 1.53, N 2.62,  $\text{Eu}(\text{pfb})_3(\text{PyPhen})$  (1 : 3), calcd, % C 41.32, H 0.79, N 5.51, found C 41.22, H 0.88, N 5.44.

**Synthesis of  $\text{Yb}(\text{pfb})_3(\text{Q})$  (Q = DPPZ, BDPZ).** The solution of  $\text{Yb}(\text{pfb})_3$  (1 mmol) in 20 ml of ethanol was added to the solutions of Q = DPPZ and BDPZ (1 mmol) in 30 ml of ethanol. The reaction mixture was refluxed for 24 h and then was evaporated to half-volume until precipitate formation. The precipitate was filtered off, washed with ethanol, and dried in air. Yield 60% of white powder  $\text{Yb}(\text{pfb})_3(\text{DPPZ})$  and 50% of orange powder  $\text{Yb}(\text{pfb})_3(\text{BDPZ})$ . – CHN:  $\text{Yb}(\text{pfb})_3(\text{DPPZ})$ , calcd, % C 43.03, H 0.93, N 5.15, found C 43.18, H 0.85, N 5.28,  $\text{Yb}(\text{pfb})_3(\text{BDPZ})$ , calcd, % C 45.36, H 1.06, N 4.92, found C 45.23, H 1.15, N 4.99.

**Synthesis of  $\text{GdCl}_3(\text{Q})$  (Q = BPhen, PyPhen, DPPZ, BDPZ).**  $\text{GdCl}_3(\text{Q})$  (Q = BPhen, PyPhen, DPPZ, BDPZ) were synthesized by reaction between solutions of  $\text{GdCl}_3$  and BPhen, PyPhen, DPPZ, and BDPZ in ethanol. The reaction mixture was refluxed for 24 h and then was evaporated to half-volume until precipitate formation. The precipitate was filtered off, washed with ethanol, and dried in air.

## Conclusions

Thus, we proposed the targeted design of efficient lanthanide-based emitters for solution-processed OLEDs, which was aimed at the combination of high luminescence efficiency with solubility and charge carrier mobility. New highly luminescent europium-based materials with PLQYs of up to 80% and purely NIR luminescent ytterbium complexes were obtained and thoroughly characterized. The HOMO and LUMO energies of solution-processed thin films of the investi-

gated complexes were measured, as well as charge carrier mobility, which has never been measured for non-volatile lanthanide complexes before. Both the proposed design of efficient lanthanide-based emitters and OLED heterostructure optimization resulted in obtaining an NIR OLED with the second highest efficiency among ytterbium-based solution-processed OLEDs ( $30 \mu\text{W W}^{-1}$ ).

## Conflicts of interest

There are no conflicts to declare.

## Acknowledgements

This work was supported by Russian Foundation for Basic Research (18-33-20210). UV thanks President's grant (MK-2799.2019.3) for financial support.

## Notes and references

- 1 N. Thejo Kalyani and S. J. Dhoble, *Renewable Sustainable Energy Rev.*, 2015, **44**, 319–347.
- 2 L. Duan, L. Hou, T.-W. Lee, J. Qiao, D. Zhang, G. Dong, L. Wang and Y. Qiu, *J. Mater. Chem.*, 2010, **20**, 6392.
- 3 L. Deng, W. Li and J. Li, *Displays*, 2013, **34**, 413–417.
- 4 T. W. Lee, T. Noh, H. W. Shin, O. Kwon, J. J. Park, B. K. Choi, M. S. Kim, D. W. Shin and Y. R. Kim, *Adv. Funct. Mater.*, 2009, **19**, 1625–1630.
- 5 L. Wang, Z. Zhao, C. Wei, H. Wei, Z. Liu and Z. Bian, *Adv. Opt. Mater.*, 2019, **7**, 1801256.
- 6 Y. Chi, T.-K. Chang, P. Ganesan and P. Rajakannu, *Coord. Chem. Rev.*, 2017, **346**, 91–100.
- 7 M. L. P. Reddy and K. S. Bejoymohandas, *J. Photochem. Photobiol., C*, 2016, **29**, 29–47.
- 8 J. Jayabharathi, K. Jayamoorthy and V. Thanikachalam, *J. Organomet. Chem.*, 2014, **761**, 74–83.
- 9 Y. Li, J. Y. Liu, Y. Di Zhao and Y. C. Cao, *Mater. Today*, 2017, **20**, 258–266.
- 10 Z. Liu, J. Qiu, F. Wei, J. Wang, X. Liu, M. G. Helander, S. Rodney, Z. Wang, Z. Bian, Z. Lu, M. E. Thompson and C. Huang, *Chem. Mater.*, 2014, **26**, 2368–2373.
- 11 S. Gong, J. Luo, Z. Wang, Y. Li, T. Chen, G. Xie and C. Yang, *Dyes Pigm.*, 2017, **139**, 593–600.
- 12 V. R. Sastri, J. R. Perumareddi, V. R. Rao, G. V. S. Rayudu and J. C. Bünzli, *Modern aspects of rare earths and their complexes*, Elsevier, Amsterdam, 2003.
- 13 V. Utochnikova, A. Kalyakina and N. Kuzmina, *Inorg. Chem. Commun.*, 2012, **16**, 4–7.
- 14 V. V. Utochnikova, A. S. Kalyakina, I. S. Bushmarinov, A. A. Vashchenko, L. Marciniak, A. M. Kaczmarek, R. Van Deun, S. Bräse and N. P. Kuzmina, *J. Mater. Chem. C*, 2016, **4**, 9848–9855.
- 15 A. S. Kalyakina, V. V. Utochnikova, E. Y. Sokolova, A. A. Vashchenko, L. S. Lepnev, R. Van Deun, A. L. Trigub,

- Y. V. Zubavichus, M. Hoffmann, S. Mühl and N. P. Kuzmina, *Org. Electron.*, 2016, **28**, 319–329.
- 16 H. Suzuki, *J. Photochem. Photobiol.*, A, 2004, **166**, 155–161.
- 17 Á. L. Álvarez and C. Coya, *Lanthanide-Based Multifunctional Materials*, Elsevier, 2018, pp. 133–170.
- 18 M. A. Katkova, A. P. Pushkarev, T. V. Balashova, A. N. Konev, G. K. Fukin, S. Y. Ketkov and M. N. Bochkarev, *J. Mater. Chem.*, 2011, **21**, 16611–16620.
- 19 T. V. Balashova, N. A. Belova, M. E. Burin, D. M. Kuzyaev, R. V. Rummyantsev, G. K. Fukin, A. P. Pushkarev, V. A. Ilichev, A. F. Shestakov, I. D. Grishin and M. N. Bochkarev, *RSC Adv.*, 2014, **4**, 35505–35510.
- 20 V. A. Ilichev, A. V. Rozhkov, R. V. Rummyantsev, G. K. Fukin, I. D. Grishin, A. V. Dmitriev, D. A. Lypenko, E. I. Maltsev, A. N. Yablonskiy, B. A. Andreev and M. N. Bochkarev, *Dalton Trans.*, 2017, **46**, 3041–3050.
- 21 A. Kovalenko, P. O. Rublev, L. O. Tcelykh, A. S. Goloveshkin, L. S. Lepnev, A. S. Burlov, A. A. Vashchenko, Ł. Marciniak, A. M. Magerramov, N. G. Shikhaliyev, S. Z. Vatsadze and V. V. Utochnikova, *Chem. Mater.*, 2019, **31**, 759–773.
- 22 T.-S. Kang, B. S. Harrison, T. J. Foley, A. S. Kniefely, J. M. Boncella, J. R. Reynolds and K. S. Schanze, *Adv. Mater.*, 2003, **15**, 1093–1097.
- 23 T.-S. Kang, B. S. Harrison, M. Bouguettaya, T. J. Foley, J. M. Boncella, K. S. Schanze and J. R. Reynolds, *Adv. Funct. Mater.*, 2003, **13**, 205–210.
- 24 Z. Li, H. Zhang and J. Yu, *Thin Solid Films*, 2012, **520**, 3663–3667.
- 25 A. S. Kalyakina, V. V. Utochnikova, I. S. Bushmarinov, I. V. Ananyev, I. L. Eremenko, D. Volz, F. Rönicke, U. Schepers, R. Van Deun, A. L. Trigub, Y. V. Zubavichus, N. P. Kuzmina and S. Bräse, *Chem. – Eur. J.*, 2015, **21**, 17921–17932.
- 26 I. Wu, P. Wang, W. Tseng, J. Chang and C. Wu, *Org. Electron.*, 2012, **13**, 13–17.
- 27 S. K. Bharti and R. Roy, *TrAC, Trends Anal. Chem.*, 2012, **35**, 5–26.
- 28 M. Latva, H. Takalo, V.-M. Mukkala, C. Matachescu, J. C. Rodríguez-Ubis and J. Kankare, *J. Lumin.*, 1997, **75**, 149–169.
- 29 X.-N. Li, Z.-J. Wu, Z.-J. Si, L. Zhou, X.-J. Liu and H.-J. Zhang, *Phys. Chem. Chem. Phys.*, 2009, **11**, 9687–9695.
- 30 S. Zhang, G. A. Turnbull and I. D. W. Samuel, *Org. Electron.*, 2012, **13**, 3091–3096.
- 31 T. W. Canzler and J. Kido, *Org. Electron.*, 2006, **7**, 29–37.
- 32 V. V. Utochnikova, N. N. Solodukhin, A. N. Aslandukov, Ł. Marciniak, I. S. Bushmarinov, A. A. Vashchenko and N. P. Kuzmina, *Org. Electron.*, 2017, **44**, 85–93.
- 33 A. S. Kalyakina, V. V. Utochnikova, M. Zimmer, F. Dietrich, A. M. Kaczmarek, R. Van Deun, A. A. Vashchenko, A. S. Goloveshkin, M. Nieger, M. Gerhards, U. Schepers and S. Bräse, *Chem. Commun.*, 2018, **54**, 5221–5224.
- 34 K. G. von Eschwege, *Polyhedron*, 2012, **39**, 99–105.
- 35 R. Grzibovskis and A. Vembris, *Study of the P3HT/PCBM Interface Using Photoemission Yield Spectroscopy*, 2016, vol. 9895, pp. 1–8.
- 36 C. Li, M. Schwab, Y. Zhao, L. Chen, I. Bruder, I. Münster, P. Erk and K. Müllen, *Dyes Pigm.*, 2013, **97**, 258–261.
- 37 L. Zhang, S. Yue, B. Li and D. Fan, *Inorg. Chim. Acta*, 2012, **384**, 225–232.
- 38 S. Janietz, D. D. C. Bradley, M. Grell, C. Giebeler and M. Inbasekaran, *Appl. Phys. Lett.*, 1998, **2453**, 24–27.
- 39 E. Giroto, A. Pereira, C. Arantes, M. Cremona, A. J. Bortoluzzi, C. A. M. Salla, I. H. Bechtold and H. Gallardo, *J. Lumin.*, 2019, **208**, 57–62.
- 40 R. Grzibovskis, J. Latvels and I. Muzikante, *IOP Conf. Ser.: Mater. Sci. Eng.*, 2011, **23**, 12021.
- 41 A. Kokil, K. Yang and J. Kumar, *J. Polym. Sci., Part B: Polym. Phys.*, 2012, **50**, 1130–1144.
- 42 N. Karl, K. Kraft, J. Marktanner, M. Münch, F. Schatz, R. Stehle, H. Uhde, F. Schatz, R. Stehle and H. Uhde, *J. Vac. Sci. Technol.*, A, 1999, **17**, 2318–2328.
- 43 H. Sirringhaus, P. J. Brown, R. H. Friend, M. M. Nielsen, K. Bechgaard, B. M. W. Langeveld-Voss, A. J. H. Spiering, R. A. J. Janssen, E. W. Meijer, P. Herwig and D. M. de Leeuw, *Nature*, 1999, **401**, 685–688.
- 44 S. H. Rhee, K. b. Nam, C. S. Kim, M. Song, W. Cho, S.-H. Jin and S. Y. Ryu, *ECS Solid State Lett.*, 2014, **3**, R19–R22.
- 45 X. Zhang, X. Guo, Y. Chen, J. Wang, Z. Lei, W. Lai, Q. Fan and W. Huang, *J. Lumin.*, 2015, **161**, 300–305.
- 46 A. A. Coelho, *J. Appl. Crystallogr.*, 2003, **36**, 86–95.
- 47 Bruker, *TOPAS 4.2 User Manual*, Bruker AXS GmbH, Karlsruhe, Germany, 2009.
- 48 J. C. De Mello, H. F. Wittmann and R. H. Friend, *Adv. Mater.*, 1997, **9**, 230–232.
- 49 E. O. Kane, *Phys. Rev.*, 1962, **127**, 131–141.
- 50 C. W. Ow-yang, J. Jia, T. Aytun, M. Zamboni, A. Turak, K. Saritas and Y. Shigesato, *Thin Solid Films*, 2014, **559**, 58–63.
- 51 H. Monjushiro, I. Watanabe and Y. Yokoyama, *Anal. Sci.*, 1991, **7**, 543–547.
- 52 K. Kanai, M. Honda, H. Ishii, Y. Ouchi and K. Seki, *Org. Electron.*, 2012, **13**, 309–319.
- 53 Y. Gao, *Mater. Sci. Eng., R*, 2010, **68**, 39–87.
- 54 E. A. Silinsh and V. Capek, *Organic Molecular Crystals, Interaction, localization and transport phenomena*, AIP Press, New York, 1994.
- 55 A. Armin, G. Juska, M. Ullah, M. Velusamy, P. L. Burn, P. Meredith and A. Pivrikas, *Adv. Energy Mater.*, 2014, **4**, 1300954.
- 56 V. V. Malov, T. Ghosh, V. C. Nair, M. M. Maslov, K. P. Katin, K. N. N. Unni and A. R. Tameev, *Mendeleev Commun.*, 2019, **29**, 218–219.
- 57 C. Wang, L. Lystrom, H. Yin, M. Hetu, S. Kilina, S. A. McFarland and W. Sun, *Dalton Trans.*, 2016, **45**, 16366–16378.
- 58 A. Delgadillo, P. Romo, A. M. Leiva and B. Loeb, *Helv. Chim. Acta*, 2003, **86**, 2110–2120.
- 59 W. Yang, W. Yang, W. Liu and W. Qin, *Spectrochim. Acta, Part A*, 2013, **104**, 56–63.